Nanoscale

Accepted Manuscript

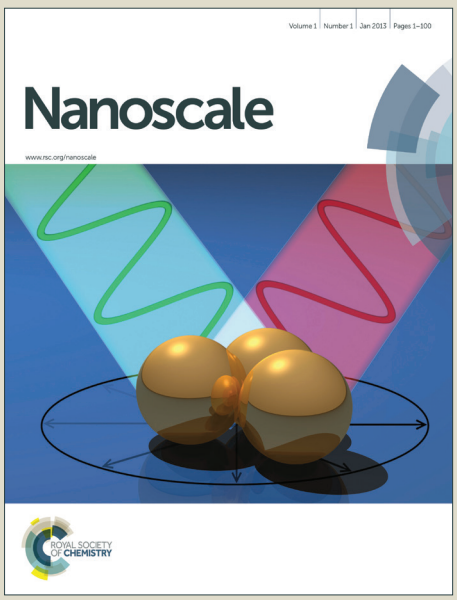

ROYAL SOCIETY OF CHEMISTRY

www.rsc.org/nanoscale

Cite this: DOI: 10.1039/c0xx00000x

www.rsc.org/xxxxxx

Paper

igh Performance Electrocatalyst Consisting of CoS Nanoparticles on an Organized Mesoporous SnO_2 Film: Use as Counter Electrodes for Pt-free, Dye-sensitized Solar Cells

Jung Tae Park,[a,b] Chang Soo Lee [a] and Jong Hak Kim [a*]

Received (in XXX, XXX) Xth XXXXXXXXX 20XX, Accepted Xth XXXXXXXXX 20XX
DOI: 10.1039/b000000x

High energy conversion efficiencies of 6.6% and 7.5% are demonstrated in solid-state and liquid-state, Pt-free dye-sensitized solar cells (DSSCs), respectively, based on CoS nanoparticles on an organized mesoporous SnO_2 (om-SnO_2) counter electrode. These results correspond to improvements of 14% and 9%, respectively, compared to a conventional Pt counter electrode and are among the highest values reported for Pt-free DSSCs. The om-SnO_2 layer plays a pivotal role as a platform to deposit a large amount of highly electrocatalytic active CoS nanoparticles via a facile solvothermal reaction. The om-SnO_2 platform with a high porosity, larger pores, and good interconnectivity is derived from a poly(vinyl chloride)-g-poly(oxyethylene methacrylate) (PVC-*g*-POEM) graft copolymer template, which provides not only improved interaction sites for the formation of CoS nanoparticles but also enhanced electron transport. The structural, morphological, chemical, and electrochemical properties of CoS on the om-SnO_2 platform are investigated using field emission-scanning electron microscopy (FE-SEM), transmission electron microscopy (TEM), Fourier transform infrared spectroscopy (FT-IR), X-ray diffraction (XRD), X-ray photoelectron spectroscopy (XPS), electrochemical impedance spectroscopy (EIS), and cyclic voltammetry (CV) measurements. The performance enhancement results from the excellent electron transport at the fluorine-doped tin oxide (FTO)/counter electrode/electrolyte interface, reduced resistance at the FTO/CoS interface, and better catalytic reduction at the counter electrode/electrolyte interface.

1. Introduction

Dye-sensitized solar cells (DSSCs) are promising devices as they are expected to provide a solution to global warming and energy source issues due to their low cost, easy fabrication, and relatively high efficiency compared to conventional silicon-based solar cells.[1] Considerable efforts have been made to improve their cell efficiency and stability based on functional photoanode materials,[2-5] an efficient redox electrolyte,[6,7] novel sensitizers with large absorption coefficients,[8] and a flexible substrate.[9] In particular, the counter electrode is not only an essential component of DSSCs due to its high cost but it also plays a significant part in determining the cell performance because the electrons that are supplied through the counter electrode have to be sufficient to reduce the redox electrolyte couples that are oxidized for sensitizer regeneration. Hence, an ideal counter electrode must possess a high electrical conductivity for the electron collecting, a large specific surface area for the counter electrode/electrolyte contact, and excellent catalytic activity for the reaction of electrolyte. In this respect, platinum (Pt) has been recognized as the most suitable counter electrode in DSSCs due to its superior electrocatalytic activity, high electrical conductivity, and good stability.[10,11] Nevertheless, the Pt counter electrode is one of the most expensive components of a DSSC and hence, may pose problems in large scale manufacturing. Therefore, the fabrication of counter electrodes based on Pt-free, low-cost, and highly catalytic active materials is essential for future industrial applications of DSSCs.[12-15]

Potential alternative counter electrode materials to replace conventional Pt should be endowed with a high electrocatalytic activity, electrical conductivity, stability, and low cost. To address these constraints, several alternative materials such as carbon,[16] carbon nanotubes,[17] metal oxide,[18] metal nitride,[19] graphene,[20], conductive polymer[21(a)] and metal chalcogenide[21(b,c)] have been investigated. Recently, our group reported an electrostatic self-assembly process for the preparation of nickel sulfide with a high catalytic activity for use as counter electrodes in DSSCs.[22] The reduced interfacial resistance at the fluorine-doped tin oxide (FTO)/counter electrode/electrolyte as well as the greater electrocatalytic activity of nickel sulfide leads to an improved fill factor and thus, a higher efficiency than conventional Pt counter electrode systems. Furthermore, their low temperature procedure capability results in enormous potential for their use in flexible photovoltaic systems. In recent years, cobalt sulfides (CoS) have also been proposed for the counter electrode of DSSCs due to their excellent electrocatalytic ability. For example, the Ho group prepared CoS acicular nanorod arrays

on a FTO substrate *via* a two-step approach and obtained a slightly lower efficiency (7.67%) than that of a conventional Pt counter electrode system (7.70%).[23] The Tuan group also achieved a high device performance of 7% by using Co_9S_8 nanocrystals as a cost-effective counter electrode material in DSSCs.[24] Very recently, the Yu group reported that CoS hierarchical nanospheres in the counter electrode in DSSCs showed higher catalytic properties.[25] However, it is still challenging to employ a simple process to prepare CoS catalysts with excellent electrocatalytic properties, a higher density, and greater surface area as a low-cost alternative to Pt in DSSCs.

Of particular interest are organized mesoporous structures with a higher crystalline framework, larger specific surface area, and tunable pores which make them ideal candidates for photovoltaic related applications such as DSSCs. For example, the Snaith group reported a bi-continuous, well-organized TiO_2 photoanode structure based on the poly(isoprene-b-styrene-b-ethylene oxide) triblock copolymer, which exhibited a higher photovoltaic performance than that of a less-organized nanoparticle based system.[26] The Wu group prepared a Pt-impregnated mesoporous Nb-doped TiO_2 structure for use as a catalytic activity enhanced counter electrode.[27] Also, our group recently reported an organized mesoporous SnO_2 interfacial layer on the FTO substrate templated by a graft copolymer, *i.e.,* poly(vinyl chloride)-*g*-poly(oxyethylene methacrylate) (PVC-*g*-POEM).[28(a)] More recently, well-organized mesoporous structures with a higher crystalline framework, larger specific surface area, and tunable pore demonstrated an excellent photoanode in DSSSs due to its high porosity, ordered pores, interconnectivity, and light harvesting.[28(b)] One way to further enhance the device performance is the application of an organized mesoporous SnO_2 film to the counter electrode, which can improve the electron transport and reduce interfacial resistance. Additionally, organized mesoporous SnO_2 structures have plenty of coordinative interaction sites such as hydroxyl groups which serve as a platform to facilitate the nucleation and successful growth of catalytic materials. It is well known that electron mobility of SnO_2 (100~200 cm^2/VS) is comparable to conventional FTO substrates, which is responsible for enhanced electron transport and minimized interfacial charge recombination.[28 (c,d)] Also, the SnO_2 nanostructure on the FTO substrates can negate interfacial charge recombination effects due to the homo-junction relation (SnO_2/F-doped SnO_2). Therefore, it is highly desirable to develop an organized mesoporous SnO_2 platform with a high porosity, larger pores, good interconnectivity, and large surface area to achieve a low-cost counter electrode with a high energy conversion performance.

Thus, in this work, we report low-cost and highly electrocatalytic active CoS nanoparticles on an organized mesoporous SnO_2 (om-SnO_2) layer as an alternative to the conventional Pt counter electrode in DSSCs. The key advantages of our suggested structure include: (1) the om-SnO_2 platform has a well-organized structure, which is beneficial to the increased electron transport and reduced interfacial resistance, (2) the om-SnO_2 platform has plenty of coordinative interaction sites (*i.e.* hydroxyl groups), a feature which is essential for facilitating the nucleation and growth of CoS nanoparticles, and (3) the highly electrocatalytic active CoS nanoparticles allow for facile electrolytic reduction at the counter electrode/electrolyte interface. The om-SnO_2 platform was synthesized *via* a sol-gel process using a graft copolymer template. Then, the as-prepared om-SnO_2 platform offered nucleation sites for CoS nanoparticles in the solverthermal step. The structural, morphological, chemical, and electrochemical properties of the CoS nanoparticles on om-SnO_2 films were characterized in detail using field emission-scanning electron microscopy (FE-SEM), transmission electron microscopy (TEM), Fourier transform infrared spectroscopy (FT-IR), X-ray diffraction (XRD), X-ray photoelectron spectroscopy (XPS), and cyclic voltammetry (CV) measurements. The resultant CoS on om-SnO_2 platform was used as a counter electrode in DSSCs and their photovoltaic performances were characterized by current density-voltage (J-V) curves and electrochemical impedance spectroscopy (EIS).

2. Results and Discussion

Synthesis and characterization of the CoS on an om-SnO_2 film

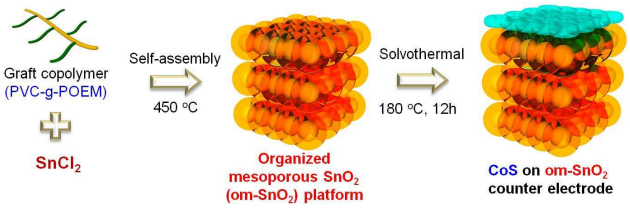

Figure 1. Schematic illustration of the preparation process of the CoS nanoparticles on om-SnO_2 platform-based counter electrode.

An effective method was developed to synthesize low-cost and highly electrocatalytic active CoS nanoparticles on an om-SnO_2 layer as an alternative to conventional Pt counter electrodes in DSSCs. The overall concept and synthesis procedure are illustrated in **Figure 1**. The crucial concept of our approach lies in the use of an om-SnO_2 film with a high porosity, larger pores, and good interconnectivity as a platform. The first step involves self-assembly of the PVC-*g*-POEM graft copolymer and $SnCl_2$ via a sol-gel reaction. The PVC-*g*-POEM graft copolymer functions as a structure directing agent due to the well-defined, microphase-separated structure in the hydrophobic, glassy PVC main chains and the hydrophilic, rubbery POEM side chains.[28(a), 29] The long molecular chains and lack of crystalinity of PVC-*g*-POEM also help to generate larger pores with a high porosity and promote the complete crystallization of SnO_2 while maintaining structural integrity. The small, hydrophilic $SnCl_2$ tin precursor provides selective interactions with the hydrophilic rubbery POEM side chains and thus, preferential confinement in the POEM domains of the PVC-*g*-POEM graft copolymer. The PVC-*g*-POEM/$SnCl_2$ hybrid undergoes microphase separation into each nanoscale domain, in which the $SnCl_2$ sol resides preferentially in the hydrophilic POEM domains separated from the hydrophobic PVC domains. Upon complete evaporation of the solvent and calcination at 450 °C, the POEM/$SnCl_2$ hybrids form a SnO_2 solid matrix with the mesopores regenerated from the isolated PVC domains. The CoS nanoparticles were *in situ* grown on the om-SnO_2 platform at 180 °C for 12 h *via* a

solverthermal method to improve the electrocatalytic activity of the counter electrode. During the solverthermal reaction, the om-SnO_2 platform provides enhanced interaction sites and facilitates the formation of CoS nanoparticles. Also, the om-SnO_2 platform would serve as a pathway to increase electron transport and reduce interfacial resistance. Thus, the CoS on om-SnO_2 counter electrode is expected to possess greater electrocatalytic activity and achieve a better performance than conventional Pt-based counter electrodes.

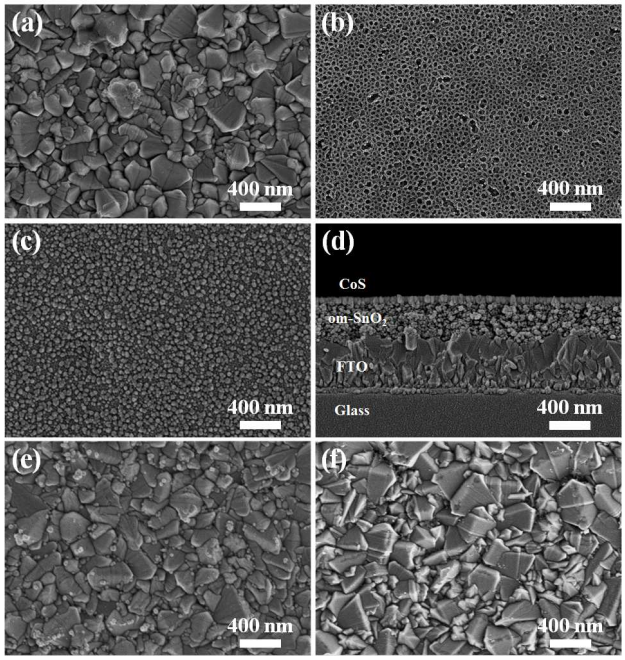

Figure 2. FE-SEM surface images of the (a) neat FTO glass substrate, (b) om-SnO_2 platform on FTO, (c) CoS on om-SnO_2/FTO counter electrode, (d) cross-sectional FE-SEM image of the CoS on om-SnO_2/FTO counter electrode, and surface images of the (e) CoS on FTO counter electrode without the om-SnO_2 platform and the (f) conventional Pt/FTO counter electrode.

The structure evolution of the CoS on om-SnO_2/FTO counter electrode was observed using FE-SEM and compared with a CoS counter electrode without the om-SnO_2 platform and a conventional Pt counter electrode, as shown in **Figure 2**. A large, cobblestone-like structure with a high surface roughness was observed for the bare FTO glass substrate (**Figure 2a)**. The om-SnO_2 platform exhibited good interconnectivity and high porosity without crack formation (**Figure 2b)**. This represents that the sol-gel synthesis with PVC-*g*-POEM graft copolymer self-assembly is an efficient approach to prepare a long-range, well-ordered om-SnO_2 film with a pore diameter of approximately 30-40 nm, which would play a key role as a platform in enhancing the electrocatalytic performance of the counter electrode. The om-SnO_2 platform has many coordinative interaction sites (*i.e.* hydroxyl groups) on the surface which would facilitate the nucleation and crystal growth of CoS nanoparticles more effectively. This behavior was characterized using FT-IR spectroscopy and is discussed in the next section. According to a previous study, the hydroxyl (-OH) groups on the metal oxide surface allow for facile coordinative interactions with another metal precursor, resulting in facilitated nucleation and growth of the nanostructure.[29] It is clear from the plan-view image in **Figure 2c** that the om-SnO_2 platform was completely and uniformly covered by the CoS nanoparticles with a size of approximately 25 nm. This size roughly matches the pore size of the om-SnO_2 platform, indicating that the aggregation of CoS nanoparticles is controlled by the binding effect of the om-SnO_2 platform. The cross-sectional FE-SEM image (**Figure 2d**) reveals that a thin CoS nanoparticle film with a thickness of approximately 50 nm was homogeneously deposited on the om-SnO_2 film, which is is also supported by TEM image (**Figure S1)**. However, the nanoparticle density of the CoS counter electrode prepared without the om-SnO_2 platform was much lower than that of the CoS on om-SnO_2 system, as shown in **Figure 2e.** This result demonstrates that the CoS on om-SnO_2 counter electrode provides a better opportunity to achieve improved interfacial contact between the FTO glass substrate and CoS nanoparticle due to enhanced adhesion properties. Meanwhile, the interfacial resistance of the redox electrolyte/CoS nanoparticles may be improved due to the formation of a high density catalytic structure, which is beneficial for electron transfer. The conventional Pt-based counter electrode was also prepared through Pt acid thermal decomposition. As shown in **Figure 2f**, the density of Pt nanoparticles on FTO glass was very low despite the high electrochemical catalytic activity, which may be due to its small particle size and the fact that it follows a completely different mechanism compared to CoS formation.

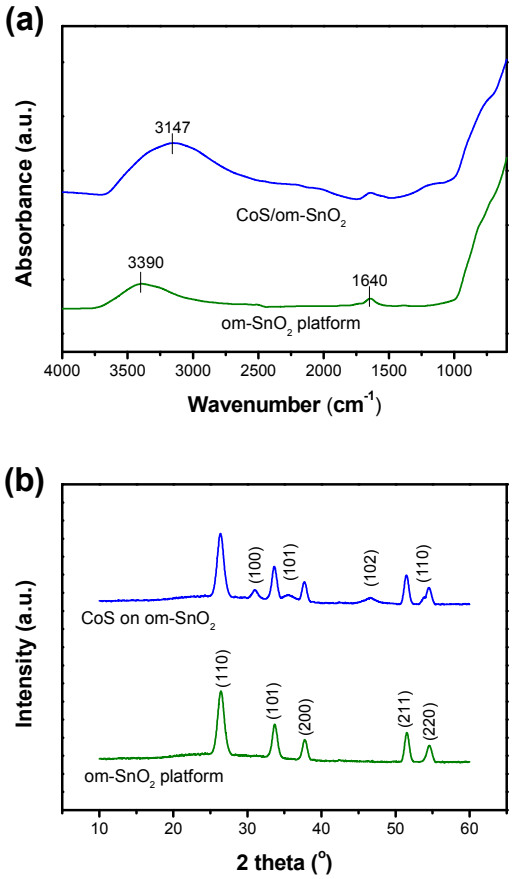

Figure 3. (a) FT-IR spectra of the om-SnO_2 platform and CoS precursor/om-SnO_2 platform before calcination, and (b) XRD patterns of the om-SnO_2 platform and CoS on om-SnO_2 counter electrode.

As mentioned in the previous FE-SEM analysis section, the numerous coordinative interaction sites (*i.e.* hydroxyl group) in the om-SnO_2 platform provide exciting possibilities to facilitate the nucleation and growth of CoS nanoparticles. To illuminate this possibility, coordinative secondary bonding interactions between the om-SnO_2 platform and the CoS precursor were investigated using FT-IR spectroscopy, as presented in **Figure 3a**. Strong absorption bands were observed at around 3,390 and 1,640 cm^{-1} in the om-SnO_2 platform, which can be attributed to -OH stretching vibrations and H-O-H bending vibrations on the metal oxide surface, respectively. Upon the introduction of CoS precursor to the om-SnO_2 platform, the -OH stretching vibration at 3,390 cm^{-1} was significantly shifted to 3,147 cm^{-1}. The peak shifts toward lower wavenumbers as a result of loosened interactions of hydroxyl groups due to coordinative interactions between the om-SnO_2 platform and CoS precursor. It is therefore concluded that facilitated nucleation and crystal growth of CoS nanoparticles with a high density result from the plentiful coordinative interaction sites (*i.e.* hydroxyl groups) present in the om-SnO_2 platform.

The crystallographic structures of the om-SnO_2 platform and CoS on om-SnO_2 counter electrode were characterized by XRD patterns, as shown in **Figure 3b**. The average size of the crystallites was calculated using the Scherrer equation shown below,

$$D = k\lambda / \beta \cos\theta$$

where D is the average size of nanoparticle crystallites, k is a shape factor of the particles (0.89), λ is the wavelength of X-ray (λ = 1.5406 Å), β is the full width at half-maximum (FWHM) of the diffraction peak, and θ is half of Bragg's diffraction angle of the centroid of the peak in degrees.[28(a)] As revealed in the XRD patterns, the om-SnO_2 platform exhibited several sharp peaks at 2θ values of 26.8, 33.99, 38.05, 52.08, and 54.66 °, which correspond to the (110), (101), (200), (211), and (220) crystal planes of the rutile SnO_2 phase, respectively (ICDD-JCPDS database, No. 41-1445). No peaks of other metal oxide species were observed in the XRD patterns, indicating a high purity of the om-SnO_2 platform. On the other hand, upon the introduction of the CoS precursor on the om-SnO_2 platform, some new peaks additionally appeared at 2θ values of 31.0, 35.5, 46.6, and 54.0, which correspond to the (100), (101), (102), and (110) planes of hexagonal CoS, respectively (ICDD-JCPDS database, No. 65-3418). The peak position and intensity of the rutile SnO_2 phase in CoS on the om-SnO_2 counter electrode were not significantly different from those of the pristine om-SnO_2 platform, indicating that the post-solverthermal treatment used for the CoS formation did not affect the crystallographic structure of the as-prepared om-SnO_2 platform. By applying the Scherrer equation, the crystallite size of CoS was calculated to be approximately 22.3 nm, which is consistent with the FE-SEM image (**Figure 2c**). These XRD results were also supported by the Co 2p and S 2p XPS spectra for the CoS on om-SnO_2, as shown in **Figure S2**. The main peak was observed with binding energies of 778.7 eV, corresponding to the binding energies of the Co 2p. The measured S 2p peaks were located at 161.5 and 162.2 eV with a spilt of 1.3 eV, which are consistent with the previously reported values.[28(e)] Therefore, this reveals that with the introduction of the CoS precursor on the om-SnO_2 platform using the post-solverthermal process, the CoS on om-SnO_2 counter electrode was successfully generated.

Photovoltaic performance of the CoS on om-SnO_2 counter electrode

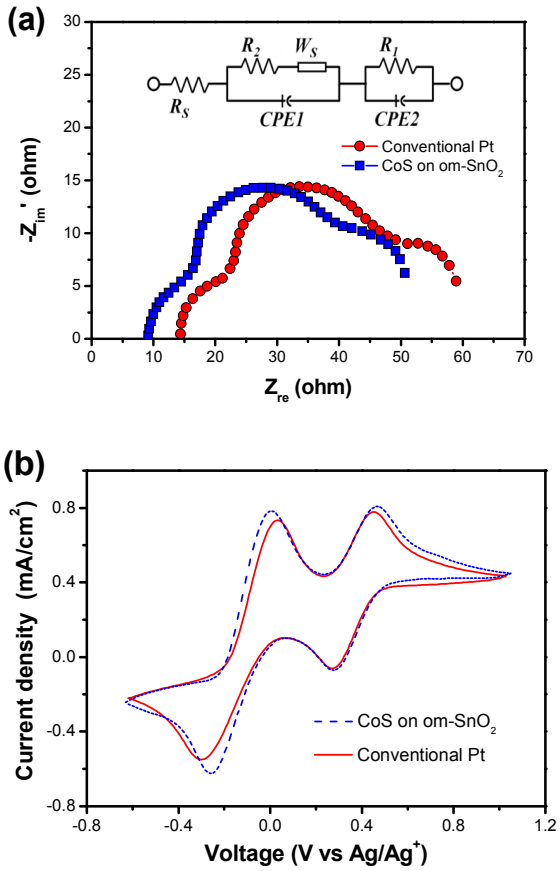

Figure 4. (a) Nyquist plots of ssDSSCs fabricated with a solid PEBII electrolyte and different counter electrodes (conventional Pt and CoS on om-SnO_2) at the open circuit condition under simulated AM 1.5G one sun light (inset: equivalent circuit diagram), (b) CV curves of the conventional Pt and CoS on om-SnO_2 counter electrodes for the redox reactions of I_2/I_3^- and I^-/I_3^-. The scan rate was 50 mVs^{-1}.

In order to further explain the variations of the photovoltaic parameters, the EIS technique was employed and the interfacial resistances in the DSSCs were analyzed. The Nyquist plots and equivalent circuit diagram of the DSSCs are shown in **Figure 4a**. The EIS Nyquist plots of the two devices (*i.e.* conventional Pt and CoS on om-SnO_2 counter electrode systems) were measured from high (1 MHz) to low frequency (0.01 Hz) at the open-circuit

voltage (V_{oc}) of each device under one sun illumination. An equivalent circuit diagram was utilized to identify the ohmic series resistance of the substrate (R_S), charge-transfer resistance (R_1, R_2, and W_S), and the corresponding constant-phase angle element (*CPE*) in the DSSCs. In general, the ohmic serial resistance (R_S) corresponds to the overall series resistance. The high frequency semicircle indicates the electrochemical impedance at the FTO substrate/countereletrode/redox electrolyte interface (R_1), while the combined semicircle in the intermediate and low frequency regions indicates impedance by the photoanoode/dye/electrolyte (R_2) interface related to the charge transport/recombination and Warburg diffusion process in the electrolyte (*Ws*), respectively.[29] In this regard, we focused mostly on the analysis of the ohmic series resistance of the substrate (R_S) and electrochemical impedance at the FTO substrate/countereletrode/redox electrolyte interface (R_1) of our suggested system. Because the same photoanode and electrolyte were used for each cell, the differences of the ohmic series resistance and impedance at the FTO substrate/countereletrode/redox electrolyte interface are responsible for the different electrochemical properties of the DSSCs. As shown in **Figure 4a**, the R_S and R_1 values of the CoS on om-SnO_2 counter electrode-based cell were lower (9.1 and 5.4 Ω) than those of the conventional Pt counter electrode-based cell (14.4 and 6.8 Ω), respectively. This result implies that the CoS on om-SnO_2 counter electrode could reduce the interfacial resistance between the FTO substrate and CoS nanoparticles due to enhanced adhesion properties. Similar observation was previously reported regarding the influence of the functional SnO_2 layer on the resistance properties in DSSCs.[28(d)] It indicates that the electron transport of the CoS on om-SnO_2 counter electrode is greater than that on the conventional Pt counter electrode at the FTO substrate/countereletrode/redox electrolyte interface due to the higher density and larger active surface area of the catalytic structure, which improves the redox electrolyte reaction. As a result, the small observed R_S and R_1 values for our suggested system imply that the electrochemical properties of the device are improved substantially when it is used as a counter electrode for DSSCs.

The electrocatalytic properties of the CoS on om-SnO_2 counter electrode with respect to the I^-/I_3^- redox couple were investigated by conducting CV measurements. As shown in **Figure 4b,** the CV curve of the CoS on om-SnO_2 counter electrode system shows two pairs of I^-/I_3^- redox peaks. The I^-/I_3^- redox peaks (1, 2) at the more negative potential correspond to the reactions in equation (1, 2) and the I^-/I_3^- redox peaks (3, 4) at the more positive potential correspond to the reactions in equation (3, 4).[30]

$I_3^- + 2e^- \rightarrow 3I^-$ (1) : cathodic peak 1
$3I^- \rightarrow I_3^- + 2e^-$ (2) : cathodic peak 2
$3I_2 + 2e^- \rightarrow 2I_3^-$ (3) : anodic peak 1
$2I_3^- \rightarrow 3I_2 + 2e^-$ (4) : anodic peak 2

Furthermore, the peak to peak separation (E_{pp}), which is inversely proportional to the standard electrochemical rate constant of the I^-/I_3^- redox reaction, is a significant factor in analyzing the catalytic activity of the counter electrode in DSSCs. The CoS on om-SnO_2 counter electrode system has a smaller E_{pp} (259 mV) than the conventional counter electrode (330 mV), indicating that the intrinsic electrocatalytic activity of the I^-/I_3^- redox reaction in the former is higher than in the latter. It should also be noted that the CoS on om-SnO_2 counter electrode system shows higher cathodic peak current densities than the conventional Pt counter electrode. This observation implies that a higher electrocatalytic surface area can be achieved in our suggested system. On the other hand, it is well known that the V_{oc} value in DSSCs lies between the potential of the photoanode and the I^-/I_3^- redox equilibrium potential of the electrolyte. In this regard, based on the condition of the same photoanode, it is expected that the V_{oc} value depends on the I^-/I_3^- redox equilibrium potential of the counter electrode system.[31] Therefore, the effect of CoS catalytic materials with the SnO_2 platform on the photovoltaic performance will be intensively discussed in the following section.

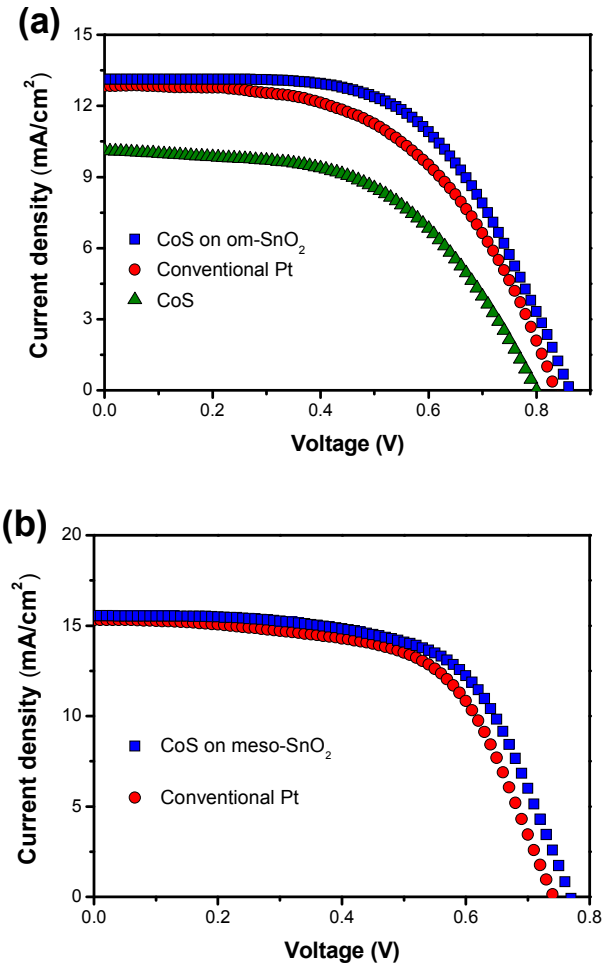

Figure 5. *J-V* curves of (a) ssDSSCs fabricated with a solid PEBII electrolyte and various counter electrodes, (b) liquid electrolyte DSSCs fabricated with conventional and CoS on om-SnO_2 counter electrodes under one sun illumination (AM 1.5, 100 mWcm^{-2}).

To investigate the effect of the catalytic properties on the

photovoltaic performance, the CoS on om-SnO_2 counter electrode was subsequently assembled into DSSCs and compared with devices fabricated using a conventional Pt counter electrode. Compared to the DSSCs with a liquid-state electrolyte, a solid-state electrolyte exhibits some advantages such as superior long-term stability, cell flexibility, and being lightweight. Thus, ssDSSCs were also fabricated using poly(1-((4 ethenylphenyl)methyl)-3-butyl-imidazolium iodide) (PEBII) as the solid electrolyte without any additives such as iodine (I_2) or an ionic liquid. The current density-voltage (*J-V*) curves measured under a simulated AM 1.5 G illumination intensity of 100 $mWcm^{-2}$ are shown in **Figure 5**. The photovoltaic parameters of the DSSCs are listed in **Tables 1 and 2**.

Table 1. Photovoltaic properties of ssDSSCs fabricated with a solid PEBII electrolyte and various counter electrodes at 100 mW/cm^2 (AM 1.5).

Counter electrode	*Voc* (V)	*Jsc* (mA/cm^2)	*FF*	η (%)
Conventional Pt	0.83	12.8	0.54	5.8
CoS	0.80	10.1	0.53	4.3
CoS on om-SnO_2	0.86	13.1	0.58	6.6

The ssDSSCs fabricated with the conventional Pt counter electrode resulted in a cell efficiency of 5.8%, while the efficiency of the CoS on om-SnO_2 counter electrode DSSC reached 6.6%. This result corresponds to a 14% efficiency improvement relative to the conventional Pt cell and is one of the highest values obtained for Pt-free, N719 dye-based ssDSSCs.[32-34] In particular, both the fill factor (*FF*) and V_{oc} were found to increase for the device with the CoS on om-SnO_2 counter electrode compared to those of the device with a conventional Pt counter electrode, which results in the enhancement of the photovoltaic performance in our suggested system. As previously demonstrated by the EIS analysis, the CoS on om-SnO_2 counter electrode exhibited a densely packed catalytic structure and has an enhanced adhesion layer to the FTO substrate. This apparently led to an increase of the electron transport at the FTO substrate/countereletrode/redox electrolyte interface and a reduction of the interfacial resistance between the FTO substrate and CoS nanoparticles, resulting in a high *FF*. In addition, the V_{oc} values suggest that CoS on om-SnO_2 counter electrodes are more effective than conventional counter electrodes in catalyzing the reduction of triiodide to iodide. The improved electrocatalytic activity and electrocatalytic surface area in the counter electrode strongly influence the rapid release of I^- species from the electrolytic reduction at the counter electrode/electrolyte interface, which agrees with the previously discussed CV analysis. The short circuit current density (J_{sc}) values were not significantly different between the conventional Pt and CoS on om-SnO_2 counter electrode systems, indicating a small effect of the modified counter electrode on the light harvesting properties. The ssDSSCs fabricated using the CoS counter electrode without the om-SnO_2 platform exhibited an energy conversion efficiency of 4.3%, indicating the importance of the om-SnO_2 platform. It should be noted that the CoS on om-SnO_2 counter electrode system showed significantly higher cathodic peak current densities than CoS counter electrode, implying the superior catalytic activities of the former (**Figure S3**). Furthermore, the EIS spectra reveal that the DSSC with CoS on om-SnO_2 counter electrode had a lower resistance value than the DSSC without om-SnO_2 structure, which strongly supports the pivotal role of om-SnO_2 platform in enhancing electrochemical properties (**Figure S4**). On the other hand, the ssDSSCs fabricated with the CoS on dense SnO_2 counter electrode showed an efficiency of only 4.0 % at 100 mW cm^{-2}, as shown in **Figure S5**. This might result from a dense SnO_2 platform with a less-interconnected particulate structure, which gives a negative impact on electron transport. Also, we observed that the dense SnO_2 platform showed less-organized structures than the om-SnO_2 platform (**Figure S6**). In addition, replacing the om-SnO_2 platform with functional SnO_2 platform is expected to improve the cell efficiency more, which is currently investigated in our lab. We also made an attempt to optimize the cell performance with the CoS on om-SnO_2 counter electrode-based DSSCs with a conventional liquid electrolyte. The liquid electrolyte consisted of 1-butyl-3-methylimidazolium iodide, I_2, guanidinium thiocyanate, and 4-tert-butylpyridine in an acetonitrile/valeronitrile mixed solvent. The device efficiency of the DSSCs using the liquid electrolyte reached 7.5% at 100 $mWcm^{-2}$, which is again higher than that (6.9%) of the conventional Pt-based system and represents one of the highest values reported for Pt-free DSSCs to date.[25,35-37] Therefore, the CoS on om-SnO_2 counter electrode demonstrates a new way to improve the performance of low-cost and highly catalytic nanomaterial-based DSSCs.

Table 2. Photovoltaic properties of liquid electrolyte-based DSSCs fabricated with the conventional and CoS on om-SnO_2 counter electrodes under one sun illumination (AM 1.5, 100 $mWcm^{-2}$). The liquid electrolyte consists of 1-butyl-3-methylimidazolium iodide, I_2, guanidinium thiocyanate, and 4-tert-butylpyridine in an acetonitrile/valeronitrile mixed solvent.

Counter electrode	*Voc* (V)	*Jsc* (mA/cm^2)	*FF*	η (%)
Conventional Pt	0.74	15.3	0.61	6.9
CoS on om-SnO_2	0.76	15.6	0.63	7.5

3. Conclusions

In summary, we developed a facile and cost effective solverthermal method to prepare a highly electrocatalytic active CoS on om-SnO_2 counter electrode for DSSC application. Using a sol-gel process with a PVC-*g*-POEM graft copolymer template, the om-SnO_2 films were generated, which play a key role as a platform in coordinating to the CoS precursor. Compared to the conventional Pt counter electrode, the CoS on om-SnO_2 counter electrode features excellent electron transport, reduced interfacial resistance, and facile electrolytic reduction in the DSSCs. Accordingly, high energy conversion efficiencies of 6.6% and 7.5% were achieved based on the CoS on om-SnO_2 counter

electrode, which correspond to improvements of 14% and 9% compared to conventional Pt-based ssDSSCs, respectively. Taking all of the mentioned properties into account, the highly electrocatalytic active CoS on om-SnO_2 counter electrode as an alternative for Pt-based conventional counter electrodes is one of the most promising strategies for low-cost energy devices with a high energy conversion performance.

4. Experimental Section

Material

Poly(vinyl chloride) (PVC, M_w = 97,000 $gmol^{-1}$, M_n = 55,000 $gmol^{-1}$), poly(oxyethylene methacrylate) (POEM, poly(ethylene glycol) methyl ether methacrylate, M_n = 475 $gmol^{-1}$), 1,1,4,7,10,10-hexamethyltriethylene tetramine (HMTETA, 99%), copper(I) chloride (CuCl, 99%), tin (II) chloride ($SnCl_2$, 99%), cobalt(II) chloride hexahydrate ($CoCl_2 \cdot 6H_2O$), thiourea (CH_4N_2S), ethylene glycol, chloroplatinic acid hexahydrate (H_2PtCl_6), titanium(IV) bis(ethyl acetoacetato) diisopropoxide, 1-butyl-3-methylimidazolium iodide, iodine (I_2), guanidinium thiocyanate, 4-tert-butylpyridine, 1-butylimidazole, 4-chloromethylstyrene, lithium iodide (LiI), magnesium sulfate ($MgSO_4$), and 2,2'-azobisisobutyronitrile (AIBN) were purchased from Sigma-Aldrich (St Louis, MO). Commercially available nanocrystalline SnO_2 (NC-SnO_2) was purchased from Alpha-Aesar. Tetrahydrofuran, N-methyl pyrrolidone, butanol, methanol, 2-propanol, chloroform, acetonitrile, diethylether, ethyl acetate, and valeronitrile were purchased from J.T. Baker. Deionized water (>18 MΩ·m) was obtained using a water purification system made by Millipore Corporation. Ruthenium dye (535-bisTBA, N719), TiO_2 commercial colloidal paste (Ti-Nanoxide, D20), TiO_2 commercial scattering paste (Ti-Nanoxide R/SP), and Surlyn (60 mm thick) were purchased from Solaronix, Switzerland. Fluorine-doped tin oxide (FTO) conducting glass substrates (TEC8, 8 ohms/sq, 2.3 mm thick) were purchased from Pilkington, France. All chemicals and solvents were reagent grade and used as received. Unless noted otherwise, all experiments were carried out under ambient conditions in air.

Preparation of the om-SnO_2 platform

The om-SnO_2 platform was prepared by a sol-gel method using $SnCl_2$ as a precursor and PVC-*g*-POEM graft copolymer as a structure-directing agent. The PVC-g-POEM graft copolymer consisting of a poly(vinyl chloride) backbone and poly(oxyethylene methacrylate) side chains were synthesized *via* atomic transfer radical polymerization (ATRP), according to a previously reported method.[38] Then, the as-prepared PVC-*g*-POEM graft copolymer (0.05 g) was dissolved in THF (2.5 mL). After stirring for 2 h, $SnCl_2$ (0.20 g) was then added to the graft copolymer solution. After aging for 15 min, additional deionized water (0.17 mL) was slowly added to the graft copolymer/tin precursor solution under vigorous stirring. Separately, the FTO glass substrates were rinsed with 2-propanol and chloroform each for 30 min and dried under nitrogen. Next, the solution was subsequently aged under mild stirring at room temperature for 12 h and spin-coated onto the FTO glass, baked at 50 °C for 30 min, and subsequently calcined at 450 °C for 30 min in air.

Preparation of the CoS on om-SnO_2 platform counter electrode

The CoS nanoparticle on om-SnO_2 platform-based counter electrode was prepared by slightly modifying a previously reported method.[37] In brief, 0.001 mol of $CoCl_2 \cdot 6H_2O$ and 0.0022 mol of CH_4N_2S were dissolved in 50 mL of ethylene glycol under stirring for 1 hour. Then, the mixed solutions were transferred to the as-prepared mesoporous SnO_2 platform coated FTO glass substrates placed against the wall of a Teflon-lined stainless steel autoclave at 180 °C for 12 h. After the reaction, the CoS on om-SnO_2 counter electrode was rinsed with ethanol several times and then calcined at 450°C in air. In addition, the conventional counter electrode (Pt counter electrode) was used as a control group, according to previously reported procedures.[38]

Fabrication of the photoanode

After cleaning, the FTO glass substrate was treated with titanium(IV) bis(ethyl acetoacetato) diisopropoxide as a TiO_2 block layer, followed by heating to 450 °C for 2 h, holding for 30 min, and cooling to 30 °C for 8 h. Next, TiO_2 commercial colloidal paste was screened onto the FTO glass substrate using the doctor-blade method. These samples were dried at 50 °C for 1 h, annealed at 80 °C for 1 h, and sintered at 450 °C for 30 min to develop a nanocrystalline TiO_2 film layer. Then, TiO_2 commercial scattering paste was cast onto the nanocrystalline TiO_2 layer and sintered at 450 °C for 30 min. Then, the TiO_2 film layer coated FTO glass substrate was sensitized with the 10^{-4} M ruthenium solution in ethanol at 50 °C for 2 h in a dark room. Finally, the dye-sensitized solar cell photoanodes were immersed in absolute ethanol for 5 min to remove non-adsorbed dye on the surface.

DSSC fabrication

DSSCs were fabricated using previously reported procedures.[38-41] In brief, two types of electrolytes were employed for the fabrication of the DSSCs: (1) solid-state polymerized ionic liquid, i.e., poly(1-((4 ethenylphenyl)methyl)-3-butyl-imidazolium iodide) (PEBII), and (2) liquid electrolyte consisting of 1-butyl-3-methylimidazolium iodide, iodine (I_2), guanidinium thiocyanate, and 4-tert-butylpyridine (TBP) in acetonitrile and valeronitrile. For the solid electrolyte DSSCs, an I_2-free PEBII electrolyte solution in acetonitrile was directly cast onto the photoanode. First, a 2 wt% dilute PEBII electrolyte solution was cast onto a dye-adsorbed photoanode and evaporated very slowly for easy penetration of the electrolytes through the nanopores of the TiO_2 layer. Next, a 10 wt% PEBII electrolyte solution was cast onto the photoanode and covered the counter electrode. Both electrodes were then superimposed and pressed between two glass plates to achieve slow evaporation of the solvent and a thin electrolyte layer. The cells were placed in a vacuum oven for one day for complete evaporation of the solvents and then sealed with an epoxy resin. In the case of the liquid system, the photoanode and counter electrode were sealed together in a sandwich configuration using a hot-melt 60 μm thick Surlyn film. The inter-electrode space was filled with an electrolyte by a vacuum back-filling method. The holes were sealed using a small piece of a hot-melt 60 μm thick Surlyn film

and a microscope cover slip. The liquid electrolyte was composed of 0.6 M 1-butyl-3-methylimidazolium iodide, 0.03 M I_2, 0.1 M guanidinium thiocyanate, and 0.5 M 4-tert-butylpyridine in a mixture of acetonitrile and valeronitrile (v/v, 85:15).

Characterization

The surface morphology of the CoS on om-SnO_2 counter electrodes was evaluated by a field emission-scanning electron microscope (SUPRA 55VP, Carl Zeiss). FT-IR spectra of the samples were collected using an Excalibur Series FT-IR (DIGLAB Co.) instrument at frequencies ranging from 4,000 cm^{-1} to 600 cm^{-1} at an ATR facility where 64 scans were signal-averaged at a resolution of 4 cm^{-1}. The phase identification of the specimens was conducted by employing X-ray diffraction (XRD) using a Rigaku with CuKα radiation (λ = 1.5406 Å) at 40 kV and 300 mA. Data were collected with a step interval of 0.1 ^{o} and a measuring time of 2 s per point in the 2 theta range of 5 ^{o} to 60 ^{o}. Surface compositions of the photoanodes were investigated by X-ray photoelectron spectroscopy (XPS) using a VG Scientific ESCALAB 220 spectrometer equipped with a hemispherical energy analyzer. A nonmonochromatized Al K X-ray source (h = 1486.6 eV) was operated at 12.5 kV and 16 mA under an analyzer chamber pressure less than 10^{-6} Pa. The electrochemical impedance spectra (EIS) were measured by a potentiostat equipped with a frequency response analyzer (Compactstat, IVIUM Technologies) in the frequency range of 0.01 Hz to 0.1 MHz. The magnitude of the alternative signal was 0.2 V. The impedance parameters were determined by fitting the impedance spectra using Z-view software. The impedance measurements were carried out at the open-circuit potential under AM 1.5 (100 mW/cm^2) light illumination. Cyclic voltammetry (CV) was performed using VSP (Bio-Logic) in a conventional three-electrode electrochemical cell. The CoS on om-SnO_2 counter electrode was used as the working electrode, while a platinum wire was used as the counter electrode and Ag/Ag+ (0.01 M $AgNO_3$ + 0.1 M $LiClO_4$ in acetonitrile) as the reference electrode. All potentials are shown versus 0.1 M Ag/Ag+ in the acetonitrile reference electrode. Photocurrent-voltage measurements were performed using a Keithley model 2400 source measure unit. A class A solar simulator (ABET Technologies, model 11000) equipped with a 1,000 W xenon lamp (Oriel, 91193) was used as a light source, where the light intensity was adjusted using a certified reference Si solar cell (Fraunhofer Institute for Solar Energy System, Mono-Si + KG filter, Certificate No. C-ISE269) at a sunlight intensity of one (100 mW/cm^2). During the photocurrent-voltage measurements, the DSSCs were covered with a black mask with an aperture to avoid additional light coming through the lateral space. The photoelectrochemical performances were calculated using the following equations,

$$FF = V_{max} \cdot J_{max} / V_{oc} \cdot J_{sc} \quad (1)$$

$$\eta = V_{max} \cdot J_{max} / P_{in} \cdot 100 = V_{oc} \cdot J_{sc} \cdot FF / P_{in} \cdot 100 \quad (2)$$

where J_{sc} is the short-circuit current density (mA/cm^2), V_{oc} is the open-circuit voltage (V), P_{in} is the incident light power, FF is the fill factor, η is the overall energy conversion efficiency, and J_{max} (mA/cm^2) and V_{max} (V) are the current density and voltage in the J-V curve, respectively, at the point of maximum power output.

Acknowledgements

We acknowledge the financial support of the Active Polymer Center for Pattern Integration (2007-0056091), the Korea Center for Artificial Photosynthesis (KCAP) (2009-0093883) and the Core Research Program (2012R1A2A2A02011268).

Notes and references

[a] *Department of Chemical and Biomolecular Engineering, Yonsei University, 262 Seongsanno, Seodaemun-gu, Seoul 120-749, South Korea*
[b] *Department of Chemical Engineering, Massachusetts Institute of Technology, 77 Massachusetts Ave., 66-325, Cambridge, MA, 02139, USA*

E-mail: jonghak@yonsei.ac.kr

† Electronic Supplementary Information (ESI) available: [details of any supplementary information available should be included here]. See DOI: 10.1039/b000000x/

[1] B. O'Regan, M. Gratzel, *Nature* 1991, **353**, 737.
[2] S. Peng, L. Li, H. Tan, R. Cai, W. Shi, C. Li, S. G. Mhaisalkar, M. Srinivasan, S. Ramakrishna, Q. Yan, *Adv. Funct. Mater.* 2014, **24**, 2154.
[3] N. P. Benehkohal, G. P. Demopoulos, *ChemSusChem* 2014, **7**, 813.
[4] S. Colella, E. Orgiu, I. Bruder, A. Liscio, V. Palermo, B. Bruchmann, P. Samorì, P. Erk, *Adv. Energy Mater.* 2014, **4**, 1301362.
[5] G. B. Shan, H. Assaaoudi, G. P. Demopoulos, *ACS Appl. Mater. Interfaces*, 2011, ***3***, 3239.
[6] S. Li, L. Qiu, C. Shi, X. Chen, F. Yan, *Adv. Mater.* 2014, **26**, 1266.
[7] H. Wang, X. Zhang, F. Gong, G. Zhou, Z.-S. Wang, *Adv. Mater.* 2012, **24**, 121.
[8] T.-C. Chu, R. Y.-Y. Lin, C.-P. Lee, C.-Y. Hsu, P.-C. Shih, R. Lin, S.-R. Li, S.-S. Sun, J. T. Lin, R. Vittal, K.-C. Ho, *ChemSusChem* 2014, **7**, 146.
[9] W. Wang, Q. Zhao, H. Li, H. Wu, D. Zou, D. Yu, *Adv. Funct. Mater.* 2012, **22**, 2775.
[10] G. Calogero, P. Calandra, A. Irrera, A. Sinopoli, I. Citro, G. Di Marco, *Energy Environ. Sci.* 2011, **4**, 1838.
[11] C. Bao, H. Huang, J. Yang, H. Gao, T. Yu, J. Liu, Y. Zhou, Z. Li, Z. Zou, *Nanoscale* 2013, **5**, 4951.
[12] H. Wang, W. Wei, Y. H. Hu, *J. Mater. Chem. A* 2013, **1**, 6622.
[13] H. Wang, K. Sun, F. Tao, D. J. Stacchiola, Y. H. Hu, *Angew. Chem. Int. Ed.* 2013, **52**, 9210.
[14] W. Wei, H. Wang, Y. H. Hu, *J. Mater. Chem. A* 2013, **1**, 14350.
[15] H. Wang, Y. H. Hu, *Energy Environ. Sci.* 2012, **5**, 8182.
[16] T. Peng, W. Sun, X. Sun, N. Huang, Y. Liu, C. Bu, S. Guo, X.-Z. Zhao, *Nanoscale* 2013, **5**, 337.
[17] S. G. Hashmi, J. Halme, Y. Ma, T. Saukkonen, P. Lund, *Adv. Mater. Interfaces* 2014, **1**, 1300055.

[18] S. Yun, H. Pu, J. Chen, A. Hagfeldt, T. Ma, *ChemSusChem* 2014, **7**, 442.
[19] G.-r. Li, F. Wang, Q.-w. Jiang, X.-p. Gao, P.-w. Shen, *Angew. Chem. Int. Ed.* 2010, **49**, 3653.
[20] P.-T. Shih, R.-X. Dong, S.-Y. Shen, R. Vittal, J.-J. Lin, K.-C. Ho, *J. Mater. Chem. A* 2014, **2**, 8742.
[21] (a) X. Yin, F. Wu, N. Fu, J. Han, D. Chen, P. Xu, M. He, Y. Lin, *ACS Appl. Mater. Interfaces* 2013, **5**, 8423. (b) F. Gong, X. Xu, Z. Li, G. Zhou, Z.-S. Wang, *Chem. Commun.* 2013, **49**, 1437. (c) J. Guo, Y. Shi, Y. Chu, T.M, *Chem. Commun.* 2013, **49**, 10157.
[22] W. S. Chi, J. W. Han, S. Yang, D. K. Roh, H. Lee, J. H. Kim, *Chem. Commun.* 2012, **48**, 9501.
[23] C.-W. Kung, H.-W. Chen, C.-Y. Lin, K.-C. Huang, R. Vittal, K.-C. Ho, *ACS Nano* 2012, **6**, 7016.
[24] S.-H. Chang, M.-D. Lu, Y.-L. Tung, H.-Y. Tuan, *ACS Nano* 2013, **7**, 9443.
[25] J. Yang, C. Bao, K. Zhu, T. Yu, F. Li, J. Liu, Z. Li, Z. Zou, *Chem. Commun.* 2014, **50**, 4824.
[26] P. Docampo, M. Stefik, S. Guldin, R. Gunning, N. A. Yufa, N. Cai, P. Wang, U. Steiner, U. Wiesner, H. J. Snaith, *Adv. Energy Mater.* 2012, **2**, 676.
[27] P. Hasin, M. A. Alpuche-Aviles, Y. Li, Y. Wu, *J. Phys. Chem. C* 2009, **113**, 7456.
[28] (a) J. T. Park, S. H. Ahn, D. K. Roh, C. S. Lee, J. H. Kim, *ChemSusChem* 2014, **7**, 2037. (b) J.T. Park, W.S. Chi, S.J. Kim, D. Lee, J.H. Kim, *Sci. Rep.* 2014, **4**, 5505; DOI: 10.1038/srep05505. (c) S. Lee, J.H. Noh, H.S. Han, D.K. Yim, D.H. Kim, J.-K. Lee, J.Y. Kim, H.S. Jung, K.S. Hong, *J. Phys. Chem. C* 2009, **113**, 6878. (d) T.-T. Duong, H.-J. Choi, Q.-J. He, A.-T. Le, S.-G. Yoon, *J. Alloy Compd.* 2013, **561**, 206. (e) S.-J. Bao, Y. Li, C.M. Li, Q. Bao, Q. Lu, J. Guo, *Cryst. Growth Des.* 2008, **8**, 3745.
[29] J. T. Park, J. H. Prosser, D. J. Kim, J. H. Kim, D. Lee, *ChemSusChem* 2013, **6**, 856.
[30] A. I. Popov, D. H. Geske, *J. Am. Chem. Soc.* 1958, **80**, 1340.
[31] L. M. Peter, *Phys. Chem. Chem. Phys.* 2007, **9**, 2630.
[32] D. Hwang, D. Y. Kim, S.-Y. Jang, D. Kim, *J. Mater. Chem. A* 2013, **1**, 1228.
[33] D. Xu, C. Shi, L. Wang, L. Qiu, F. Yan, *J. Mater. Chem. A* 2014, **2**, 9803.
[34] C.-P. Lee, L.-Y. Lin, P.-Y. Chen, R. Vittal, K.-C. Ho, *J. Mater. Chem.* 2010, **20**, 3619.
[35] T.-L. Zhang, H.-Y. Chen, C.-Y. Su, D.-B. Kuang, *J. Mater. Chem. A* 2013, **1**, 1724.
[36] J. Kwon, V. Ganapathy, Y. H. Kim, K.-D. Song, H.-G. Park, Y. Jun, P. J. Yoo, J. H. Park, *Nanoscale* 2013, **5**, 7838.
[37] Y. Gu, Y. Xu, Y. Wang, *ACS Appl. Mater. Interfaces* 2013, **5**, 801.
[38] J. T. Park, W. S. Chi, D. K. Roh, S. H. Ahn, J. H. Kim, *Adv. Funct. Mater.* 2013, **23**, 26.
[39] J. T. Park, W. S. Chi, H. Jeon, J. H. Kim, *Nanoscale* 2014, **6**, 2718.
[40] S. Y. Heo, J. K. Koh, G. Kang, S. H. Ahn, W. S. Chi, K. Kim, J. H. Kim, *Adv. Energy Mater.* 2014, **4**, 1300632.
[41] S. H. Ahn, D. J. Kim, W. S. Chi, J. H. Kim, *Adv. Mater.* 2013, **25**, 4893.

Graphical Abstract

High performance electrocatalyst was prepared based on CoS nanoparticles on an organized mesoporous SnO_2 platform. High energy conversion efficiencies of 6.6 % and 7.5 % were demonstrated in solid-state and liquid-state, Pt-free dye-sensitized solar cells (DSSCs), respectively, which are much higher than those of conventional Pt-based DSSCs and are among the highest values reported for Pt-free DSSCs.